Anomalous Reynolds-number scaling in turbulent Rayleigh–Bénard convection

Eric Brown[1], Denis Funfschilling[2] and Guenter Ahlers[1]

[1] Department of Physics and iQCD, University of California, Santa Barbara, CA 93106, USA
[2] LSGC–CNRS, 1 rue Grandville, BP 451, 54000 Nancy, France
E-mail: ebrown@physics.ucsb.edu, Denis.Funfschilling@ensic.inpl-nancy.fr and guenter@physics.ucsb.edu

Abstract. This paper reports measurements of Reynolds numbers R_e^p corresponding to the turnover time of thermal excitations ('plumes') and R_e^ω corresponding to the twisting-oscillation period of the large-scale circulation (LSC) of turbulent Rayleigh–Bénard convection over the Rayleigh-number range $2 \times 10^8 \lesssim R \lesssim 10^{11}$ and Prandtl-number range $3.3 \lesssim \sigma \lesssim 29$ for cylindrical samples of aspect ratio $\Gamma = 1$. For $R < R^* \simeq 3 \times 10^9$ both periods, and hence both Reynolds numbers, were the same and scaled as $R_e \sim R^{\gamma_{\text{eff}}}$ with $\gamma_{\text{eff}} \simeq 0.45 < 1/2$. Here both the σ- and R-dependences were quantitatively consistent with the Grossmann–Lohse (GL) prediction. For $R > R^*$ the results could be represented by $R_e^p = 0.138 \ \sigma^{-0.82} R^{0.493}$ for the plume turnover time and $R_e^\omega = 0.17 \ \sigma^{-0.81} R^{0.480}$ for the twisting oscillation, both of which differ significantly from the GL prediction as well as from each other. A relatively sharp transition at R^* to the large-R regime and the separation of the two Reynolds numbers from each other suggest a qualitative and sudden change that renders the measured quantities inapplicable to the GL prediction.

Combining R_e^p and previously reported measurements of the Nusselt number $\mathcal{N}$ yielded the kinetic energy-dissipation $\epsilon_u = (\mathcal{N} - 1)R/\sigma^2$ as a function of R_e^p. For $R \lesssim R^*$ these results were in excellent agreement with the corresponding GL prediction, and both approached closely to the $(R_e)^3$-dependence that is expected at large R_e where the bulk contribution to ϵ_u dominates. For $R > R^*$ the data were consistent with $\epsilon_u \propto (R_e)^{8/3}$. This differs from the expected large-R_e behavior and suggests that R_e^p no longer is the Reynolds number relevant to ϵ_u.

Keywords: heat transfer and convection, turbulence

Contents

1. Introduction

Understanding turbulent Rayleigh–Bénard convection (RBC) in a fluid heated from below [1] remains one of the challenging problems in nonlinear physics. It is well established that a major component of the dynamics of this system is a large-scale circulation (LSC) [2]–[10]. The LSC plays an important role in many natural phenomena, including atmospheric and oceanic convection [11] and convection in the outer core of Earth [12] where it is believed to be responsible for the generation of the magnetic field.

In this paper we consider cylindrical samples of aspect ratio $\Gamma \equiv D/L \simeq 1$ (D is the diameter and L the height). For these the LSC consists of a single convection roll over a wide range of parameters, with both down-flow and up-flow near the side wall but at azimuthal locations θ that differ by π. From a theoretical viewpoint [13] it is desirable to describe its rate of circulation by a single Reynolds number, for instance by

$$R_e^{\mathrm{LSC}} \equiv \frac{2L^2}{\mathcal{T}\nu}, \tag{1}$$

where $\mathcal{T}$ is a spatially independent turnover time and ν the kinematic viscosity. No direct measurements of $\mathcal{T}$ seem to exist, but $\mathcal{T}$ has been inferred from more localized velocity measurements. For instance, the time-averaged maximum velocity v_{max} that is observed [14, 15] more or less near the region (sometimes known as the 'mixing zone' [4]) between the viscous boundary layers and the bulk of the system, combined with L as

the appropriate length scale, was used to obtain [15] $R_e^{v_{\max}} \propto v_{\max} L/\nu$. For rigid-body rotation (but not necessarily for a more complex LSC), $R_e^{v_{\max}}$ is proportional to R_e^{LSC} with $\mathcal{T} \propto L/v_{\max}$. Alternatively, the slope γ_u in the sample interior away from the mixing zone of the time-averaged horizontal component u of the LSC velocity as a function of the vertical position along the sample axis was combined with L to infer an LSC turnover time and a Reynolds number $R_e^u = \gamma_u L^2/\nu$ (similar measurements were made also of the vertical velocity component along a diameter in the horizontal mid-plane of the sample) [7, 16].

An interesting dynamical-systems property of the LSC is a twisting azimuthal oscillation mode with frequency $f_0 = \omega_0/2\pi$ that will be discussed in detail below in section 3.1. A torsional oscillation mode has been observed in the sun [17], and torsional oscillations in Earth's core are believed to cause variations in the length of the day [18]. In laboratory convection experiments, the spatial nature of this mode has become apparent only recently [8, 19], and the existence and characteristics of the mode were confirmed and extended to larger Rayleigh numbers in a recent paper [20]. Although its geometrical features long remained unclear, its frequency may have been observed or measured much earlier in a number of single-point determinations of the temperature or the velocity [21, 4, 5], [22]–[24], [7, 14, 16, 15, 25], both of which have an oscillatory contribution from the twisting mode provided the probe is not located in the horizontal mid-plane of the sample where the amplitude of this mode vanishes [20]. Some of the single-point measurements yielded results for f_0 that were equal to other estimates of $1/\mathcal{T}$ within experimental resolution [16]. The reason for this equality is not known at this time, but it suggests that the Reynolds number

$$R_e^\omega \equiv \frac{2L^2 f_0}{\nu} \tag{2}$$

is equal to R_e^{LSC}. However, some other experimental investigations indicated that there is a distinct difference between the R-dependence of $R_e^{v_{\max}}$ data obtained from velocimetry measurements of $v_{\max}$ and the R_e^ω results based on oscillation-frequency determinations [15]. Although there is no solid evidence that the single-point measurements of coherent oscillations pertain to the twisting oscillation mode, the fact that both are coherent and have the same frequency suggests that they are probably related.

An additional important component of the dynamics is the generation of localized volumes of relatively hot or cold fluid, known as 'plumes', at a bottom and a top thermal boundary layer [26, 21]. The hot (cold) plumes are carried by the LSC from the bottom (top) to the top (bottom) of the sample and by virtue of their buoyancy contribute to the maintenance of the LSC. The local vertical plume speed v_{p} was measured by several investigators by determining the transit time of temperature fluctuations between two vertically separated but closely spaced temperature probes [3, 4, 22, 27, 28]. By a similar technique, but using a single temperature sensor or two sensors on opposite sides of the sample, the plume turnover time $\mathcal{T}_{\mathrm{p}}$ was determined from peaks in time auto-correlation or cross-correlation functions of the temperature signals [29]. The plume circulation can then be characterized by a Reynolds number

$$R_e^p \equiv \frac{2L}{\mathcal{T}_{\mathrm{p}}}. \tag{3}$$

One might hope that the Reynolds number $R_e^{v_{\mathrm{p}}}$ based on the local v_{p} would be equal to the global R_e^p given by equation (3), but this need not be the case. Quite remarkably, the measurements indicate over a wide parameter range that $R_e^{v_{\mathrm{max}}} = R_e^u = R_e^p = R_e^{v_{\mathrm{p}}}$ within fairly small experimental errors. This can be interpreted to mean that the plume circulation is accurately slaved to the LSC, or vice versa, and that all of these quantities yield an accurate representation of R_e^{LSC}.

A central prediction of various theoretical models [1], [30]–[32], [13, 33] is the dependence of $R_e(R, \sigma)$ on the Rayleigh number

$$R = \frac{\beta g \Delta T L^3}{\kappa \nu} \tag{4}$$

(here β is the isobaric thermal expansion coefficient, g the acceleration of gravity, and κ the thermal diffusivity) and on the Prandtl number

$$\sigma = \frac{\nu}{\kappa}. \tag{5}$$

A recent prediction by Grossmann and Lohse (GL) [13], based on the decomposition of the kinetic and the thermal dissipation into boundary-layer and bulk contributions, has been in remarkably good agreement with many of the experimental results for $R_e^{\mathrm{LSC}}(R, \sigma)$, R_e^ω, and R_e^p in the parameter range where all three of these, so far as they have been measured, agree with each other[3]. In that regime both the prediction and the experiment can be described well by a power law $R_e \propto R^{\gamma_{\mathrm{eff}}}$ with a very slightly R-dependent effective exponent $\gamma_{\mathrm{eff}} \simeq 0.44$. However, there also are some notable differences between the predictions and some other measurements [15].

The present paper reports new measurements of $R_e^\omega(R, \sigma)$ and $R_e^p(R, \sigma)$ for R up to 10^{11} and $3.3 \lesssim \sigma \lesssim 29$. For modest R, say $R < R^* \simeq 3 \times 10^9$, there again is very good agreement with the predictions of GL and with previous experimental results. However, for $R > R^*$ the measurements reveal a relatively sudden transition to a new state of the system, with a plume Reynolds number that is described well by

$$R_e^p = R_{e,0} \; \sigma^{-\alpha} \; R^\gamma \tag{6}$$

with $R_{e,0} = 0.138 \pm 0.007$, $\alpha = 0.82 \pm 0.01$, $\gamma = 0.493 \pm 0.002$ and a twist-oscillation Reynolds number

$$R_e^\omega = R'_{e,0} \; \sigma^{-\alpha'} \; R^{\gamma'} \tag{7}$$

with $R'_{e,0} = 0.17 \pm 0.03, \alpha' = 0.81 \pm 0.03, \gamma' = 0.480 \pm 0.006$. These results differ both in the σ-dependence and in the R-dependence from the GL prediction for R_e^{LSC}. However, they agree quite well with recent experimental results for R_e^p obtained by Sun and Xia [35] in the range $7 \times 10^{10} \lesssim R \lesssim 2 \times 10^{12}$. If the GL model still correctly predicts the R-dependence of R_e^{LSC} in this parameter range, then the experimental results for R_e^p and R_e^ω suggest the existence of a new LSC state in which the plumes and the LSC are no longer slaved to each other and where the twist oscillation of the LSC is no longer synchronous with the LSC turnover time. The observation that $R_e^p > R_e^{\mathrm{LSC}}$ would then indicate that the plumes rise and fall more rapidly than the background flow of the LSC. However, as has been suggested by others, [34, 35] it seems more likely that the LSC evolves into a

---

[3] See, for instance [16] and [8], and references therein.

more complex flow structure where its dynamics can no longer be described quantitatively by a uniquely defined spatially independent Reynolds number. It is unclear at present whether the difference between this state and the one at smaller R will be found in the geometry of the flow, in the nature of the viscous boundary layers that interact with it, or in the nature and frequency of plume shedding by the thermal boundary layers adjacent to the top and bottom plates.

Another important aspect of the predictions is the dependence of the Nusselt number (the dimensionless effective thermal conductivity)

$$\mathcal{N} = \frac{QL}{\lambda \Delta T} \tag{8}$$

on R and σ (here Q is the heat-current density and λ the thermal conductivity). The GL model [32, 13] provides a good fit also to data for $\mathcal{N}$ at modest R, say up to $R \simeq 10^{10}$ [36]– [38]. Here we briefly mention as well measurements of $\mathcal{N}$ for larger R [38] that depart significantly from the GL prediction as R approaches 10^{11} and that can be described well by $\mathcal{N} \sim R^{1/3}$.

Having obtained both R_e^p and $\mathcal{N}$ as a function of R, one can also examine the averaged kinetic energy-dissipation $\epsilon_u = (\mathcal{N} - 1)R/\sigma^2$ as a function of R_e^p. There is excellent agreement with the GL prediction for ϵ_u when $R_e^p \lesssim 2000$ ($R \lesssim 3 \times 10^9$). In that range both the prediction and the data already have approached closely to the expected bulk-dominated limit in which one expects $\epsilon_u \sim R_e^3$. At larger R_e^p we find $\epsilon_u \sim (R_e^p)^{8/3}$. This is inconsistent with the expected large-R_e behavior and provides further evidence for a breakdown of the characterization of the LSC in terms of R_e^p.

2. Apparatus and experimental methods

2.1. The samples

Measurements were made for three cylindrical samples with $\Gamma \simeq 1$ [39] and known as the small, medium, and large samples. They had $L(D) = 9.52$ (9.21), 24.76 (24.81), and 50.61 (49.69) cm respectively. As is evident from equation (4), a given accessible range of ΔT will provide data over different ranges of R for the different L-values. The small sample was used to determined R_e^ω. It was filled with 2-propanol at $40.00\,^{\circ}$C ($\sigma = 28.9$). The medium and large samples were filled with water, mostly at mean temperatures $T_{\mathrm{m}} = 56.00, 40.00$, and $28.00\,^{\circ}$C corresponding to $\sigma = 3.26, 4.38, 5.68$ and $\nu = 5.15 \times 10^{-7}, 6.69 \times 10^{-7}, 8.42 \times 10^{-7}$ m^2 s^{-1} respectively. For them both R_e^ω and R_e^p were measured. The top and bottom plates were made of copper. A Plexiglas side wall had a thickness of 0.32 (0.63) cm for the medium (large) sample.

2.2. Methods of measurements

2.2.1. Small sample. In the small sample, observations of the motion of plumes across the bottom and top plate were made by means of shadowgraph imagery [8, 20, 40]. The oscillation frequency of the LSC, and from it R_e^ω, was determined from the oscillations of the path followed by the plumes as they were swept along laterally by the LSC just above the bottom or just below the top plate. This method was discussed in detail in [8] and [20].

2.2.2. Medium and large sample. For the medium and large samples, three rows of eight thermistors each, equally spaced around the circumference and labeled $i = 0, \ldots, 7$ at heights $3L/4$, $L/2$, and $L/4$ above the sample bottom, were imbedded in small holes drilled horizontally into but not penetrating the side wall, as already described elsewhere [29, 41, 20]. The thermistors were able to sense the adjacent fluid temperature without interfering with delicate fluid-flow structures. Since the LSC carried warm (cold) fluid from the bottom (top) plate up (down) the side wall, these thermistors detected the location of the up-flow (down-flow) of the LSC by indicating a relatively high (low) temperature.

To determine the orientation of the LSC, measurements with a sampling period $\delta t \simeq 2.5$ s were made, and the function

$$T_i = T_0 + \delta \cos\left(\frac{\mathrm{i}\pi}{4} - \theta_0\right), \qquad i = 0, \ldots, 7, \tag{9}$$

was fitted, separately at each time step, to the eight middle-row side-wall thermistor-temperature readings. As discussed elsewhere [42], equation (9) is an excellent representation of the time-averaged azimuthal temperature profile. The fit parameter δ is a measure of the temperature amplitude of the LSC and θ_0 is the azimuthal orientation of the plane of the LSC circulation. As defined here, the orientation θ_0 is on the side of the sample where the LSC is warm and up-flowing and is measured relative to the location of thermometer zero. Orientations θ_{t} and θ_{b} and amplitudes δ_{t} and δ_{b} were calculated for the top and bottom rows separately by the same method as for the middle row.

When a warm (cold) plume passed a given side-wall thermistor, the indicated temperature was relatively high (low). Over a certain range of R it had been shown before [16], by comparison of temperature sensors actually imbedded in the fluid and laser Doppler velocimetry, that this thermal signature can be used to determine the speed, and thus the Reynolds number R_e^p, of the plumes and that it yields the same result as actual velocity measurements for instance of R_e^u. Indeed, where there is overlap, our results for R_e^p are in satisfactory agreement with measurements [16] based on velocimetry.

From time series of the eight temperatures $T_i(t)$ taken at intervals of $\delta t \simeq 2.5$ s and covering at least one and in some cases more than ten days at each of many values of R the auto-correlation functions (ACs) $C_{i,j}(\tau), i = j$, and the cross-correlation functions (CCs) $C_{i,j}(\tau), i = 0, \ldots, 3, j = i + 4$ corresponding to signals at azimuthal positions displaced around the circle by π were determined. They are given by

$$C_{i,j}(\tau) = \langle [T_i(t) - \langle T_i(t)\rangle] \times [T_j(t + \tau) - \langle T_j(t)\rangle]\rangle. \tag{10}$$

We show an example of ACs (circles) and of CCs (squares) in figure 1.

3. Experimental results

3.1. Twisting oscillations

The same oscillations that were observed in the small sample [8] were found also in the medium and large samples. This was done by looking at time series of the LSC orientations θ_{t}, θ_0, and θ_{b} at the three different heights. An example of the time series for the three rows is shown in figure 2 for $R = 8.7 \times 10^{10}$ in the large sample. While the orientation
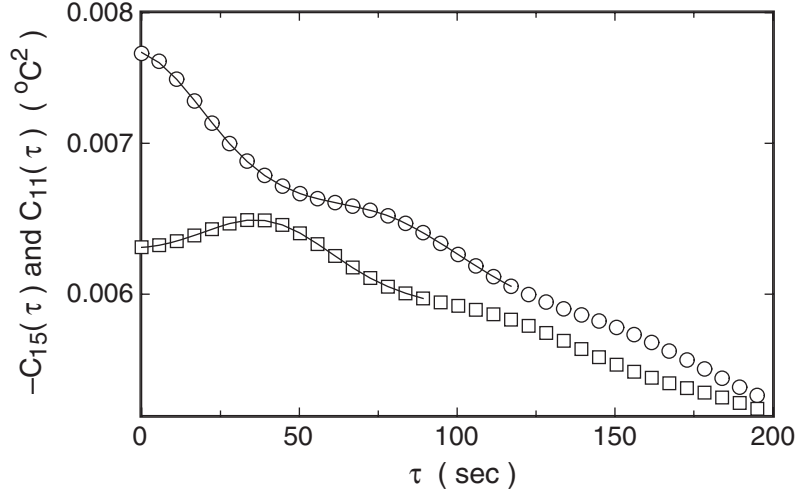
Figure 1. The CC (squares) between two thermometers (1 and 5) mounted on opposite sides of the side wall, and the AC (circles) of a single thermometer (1), on a logarithmic scale as a function of the delay time τ for the large sample and $R = 7.5 \times 10^{10}$. Solid lines: fits of equation (11) to $C_{11}(\tau)$ and of equation (12) to $C_{15}(\tau)$. The lengths of the lines indicate the range of the data used in the fits.

of each row contains erratic motion, there is a tendency for the top- and bottom-row orientations to oscillate out of phase with each other around the middle-row orientation. The frequency of this twisting oscillation was measured by fitting a Lorentzian function to each peak of the power spectra of $\theta_t - \theta_0$, $\theta_b - \theta_0$, and $\theta_t - \theta_b$. Each of these three signals gave the same peak frequency within experimental resolution. Correlation functions and power spectra are shown in [20].

3.2. Plume turnover time

From figure 1 one sees that the ACs have a peak centered at the origin. It can be represented well by a Gaussian function. The peak width indicates that the plume signal retains some correlation over a significant time interval. A second smaller Gaussian peak is observed at a later time t_2^{ac} that we identify with one turn-over time $\mathcal{T}_p$ of the plumes. The existence of this peak suggests that the plumes retain some coherence while they undergo a complete rotation. A further very faint peak is found at $2\mathcal{T}_p$, but is not used in the analysis. These observations are consistent with previous experiments [4, 43, 16]. This structure is superimposed onto a broad background that decays roughly exponentially on a timescale of $\mathcal{O}(10\mathcal{T}_p)$. We believe that the large background is caused by the slow meandering of the azimuthal orientation of the LSC.

The CCs are consistent with the ACs. Here too there is a broad, roughly exponential, background. There is no peak at the origin, and the first peak, of Gaussian shape, occurs at a time delay $t_1^{cc} = \mathcal{T}_p/2$ associated with half a circulation period. A further peak is observed at $3\mathcal{T}_p/2$, corresponding to 1.5 circulation periods. The fact that the CC is *negative* indicates that the peaks are not simply due to plume circulation from
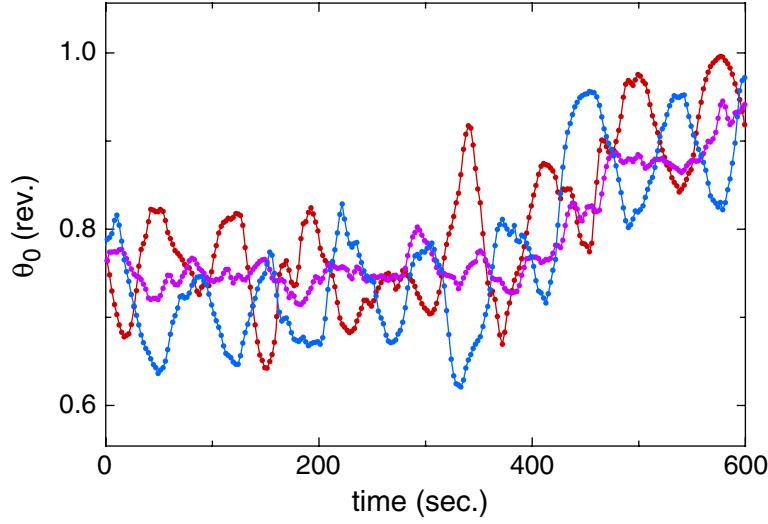
Figure 2. The mean wind orientation calculated separately for the three planes of thermistors at $R = 8.7 \times 10^{10}$ in the large sample. Red: bottom row. Purple: middle row. Blue: top row. The top-row and bottom-row orientations were observed to oscillate around the middle-row orientation.

which one would expect a positive correlation. A model due to Villermaux [44] invokes a more intricate mechanism than simple plume circulation for the coherence of the plume signal, resulting in the emission of plumes alternately from the top and bottom boundary layers. This model suggests that a warm plume on one side of the sample is followed by a cold plume on the opposite side, consistent with the negative correlation observed in the measurements.

Based on the above, the equation

$$C_{i,i}(\tau) = b_0 \exp\left(-\frac{\tau}{\tau_0^{\mathrm{ac}}}\right) + b_1 \exp\left[-\left(\frac{\tau}{\tau_1^{\mathrm{ac}}}\right)^2\right] + b_2 \exp\left[-\left(\frac{\tau - t_2^{\mathrm{ac}}}{\tau_2^{\mathrm{ac}}}\right)^2\right] \tag{11}$$

was fitted to the data for the ACs, and the equation

$$C_{i,j}(\tau) = -b_0 \exp\left(-\frac{\tau}{\tau_0^{\mathrm{cc}}}\right) - b_1 \exp\left[-\left(\frac{\tau - t_1^{\mathrm{cc}}}{\tau_1^{\mathrm{cc}}}\right)^2\right] \tag{12}$$

to those for the CCs. Examples of the fits are shown in figure 1 as solid lines. One sees that they are excellent.

As an illustration of the statistical errors involved in the analysis, figure 3 shows the results for t_1 obtained by fitting equation (12) to data for $C_{i,j}$ for one particular run at $R = 2.4 \times 10^{10}$ and $\sigma = 4.38$. They yield a mean value of 71.3 s, with a standard deviation $\sigma_{\mathrm{t1}} = 1.5$ s. The statistical errors for individual points are typically an order of magnitude smaller. It is not clear if the scatter in the data of figure 3 may be due to the turbulent fluctuations in the fluid which have not been averaged out completely over the duration of the run, or to some systematic errors that depend on the azimuthal orientation. Treating σ_{t1} as a statistical uncertainty, one expects the mean over the eight
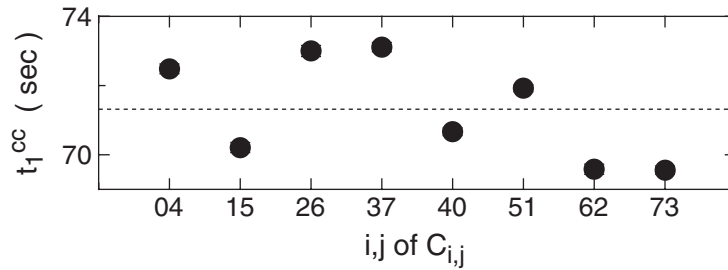
Figure 3. Results for t_1^{cc} from fits of equation (12) to the data for the temperature CCs $C_{i,j}$ for $R = 2.43 \times 10^{10}$ for the large sample. The standard error from each fit is about as large as the data points in the figure. The much larger scatter is attributable to the turbulent nature of the flow and the finite length of the experimental time series.

CCs to have an uncertainty of about 0.6 s or 0.8% if the scatter is random. Indeed, the $R_e/R^{1/2}$ data for the large sample and a Prandtl number of 4.38 to be shown below in figure 5(b) yield a mean value of 0.0347 with a standard deviation of 3.0×10^{-4} or 0.9%, consistent with the above analysis of the particular example represented by figure 3.

To check that the fitting function equation (12) does not give a biased turn-over time due to the large, decaying background, the same analysis was done on data from a sample that was deliberately tilted relative to gravity. The tilt locks in a preferred orientation of the LSC so that the warm fluid in the bottom boundary layer flows up-slope along the bottom plate due to buoyant forces [29]. Similarly cold fluid in the top boundary layer flows down-slope. This flow locking had the effect of strengthening the LSC and making the temperature oscillations at a point more coherent so that the decay of the oscillations in the correlation function is slower and can be detected for τ up to the duration of the experiment. The long-term correlation makes it possible to obtain the plume turnover rate from Fourier-transform methods. This is shown in figure 4. This value agreed with the turnover time obtained from fitting equation (12) to the $C_{i,j}$ from the same dataset within the experimental resolution of 1% for several tilt angles up to 12°, where the turnover time is shorter than the level-sample value by about 20% [29]. This agreement confirms that the background of the fitting function does not bias the measurement of the turnover time.

3.3. Reynolds numbers

To obtain experimental measures of the plume-turnover Reynolds number R_e^p, the average value of the half-turnover time $\langle t_1^{cc} \rangle$ of the eight CCs $C_{i,j}$ and $C_{j,i}$ with $i = 0, \ldots, 3$ and $j = i+4$, and the average value of $\langle t_2^{ac} \rangle$ of the eight ACs $C_{i,i}$ with $i = 0 \ldots 7$ were computed for each R. Substituting $\mathcal{T}_p = t_2^{ac}$ and $\mathcal{T}_p = 2t_1^{cc}$ into equation (3), one gets

$$R_e^{p,ac} = \frac{2}{\langle t_2^{ac} \rangle} \frac{L^2}{\nu} \tag{13}$$
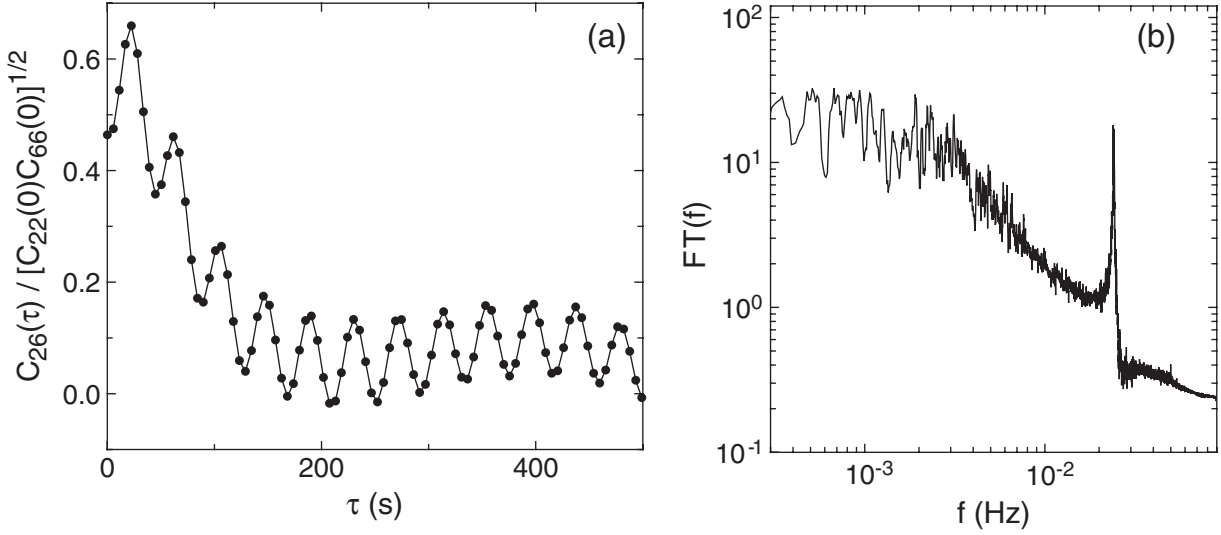
Figure 4. (a) Results for $C_{26}(\tau)$ for $R = 1.1 \times 10^{10}$ for the medium sample with a tilt of $12°$. The correlation function becomes more coherent when the sample is tilted. (b) The modulus of the Fourier transform $FT(f)$ of $C_{26}(\tau)$, revealing a sharp peak corresponding to $1/\mathcal{T}$.

and

$$R_e^{p,\text{cc}} = \frac{1}{\langle t_1^{\text{cc}} \rangle} \frac{L^2}{\nu} \qquad (14)$$

as two experimental estimates of R_e^p.

The results are shown in figure 5(a) as black circles for $R_e^{p,\text{cc}}$ and green circles for $R_e^{p,\text{ac}}$. Figure 5 shows excellent agreement between the ACs and the CCs, confirming that the analysis method gives consistent results. The data for R_e^ω from the small sample deduced from the oscillation of the direction of plume motion across the bottom plate [8] are shown as stars. These data are for 2-propanol with $\sigma = 28.9$. For comparison, the results of Qiu and Tong [16][4] for R_e^u based on velocity measurements using water with $\sigma = 5.4$ are shown as plusses. They fall near our data for $\sigma = 5.55$, showing the agreement between R_e^p and R_e^u for this range of R. The dashed lines in figure 5 are, from top to bottom, the predictions of GL [13] for $\sigma = 3.32$, 4.38, and 5.55.[5] For $R < R^* \simeq 3 \times 10^9$ they pass very well through the data. We regard this agreement of the prediction with the measurements as a major success of the model. A significant departure from the GL prediction is that for $R > R^*$ the data for the reduced Reynolds number $R_e/R^{1/2}$ scatter randomly about the horizontal solid lines, indicating that the exponent of the power-law

[4] The data points of Qui and Tong [16] at their largest R-values correspond to values of ΔT approaching $60\,°$C and may be influenced by non-Boussinesq effects. In addition, they were taken at a somewhat higher mean temperature than the others (Qiu, private communication) and thus correspond to a σ-value somewhat smaller than 5.4.

[5] We changed the parameters of the GL model to read $c_1 = 10.16$, $c_2 = 1.832$, $c_3 = 0.478$, $c_4 = 0.0141$, $a = 0.464$, $Re_c = 0.925$ to fit our R_e^ω data for $\sigma = 28.9$. This gives a better fit to our R_e data and does not alter the prediction for $\mathcal{N}(R, \sigma)$ [13].
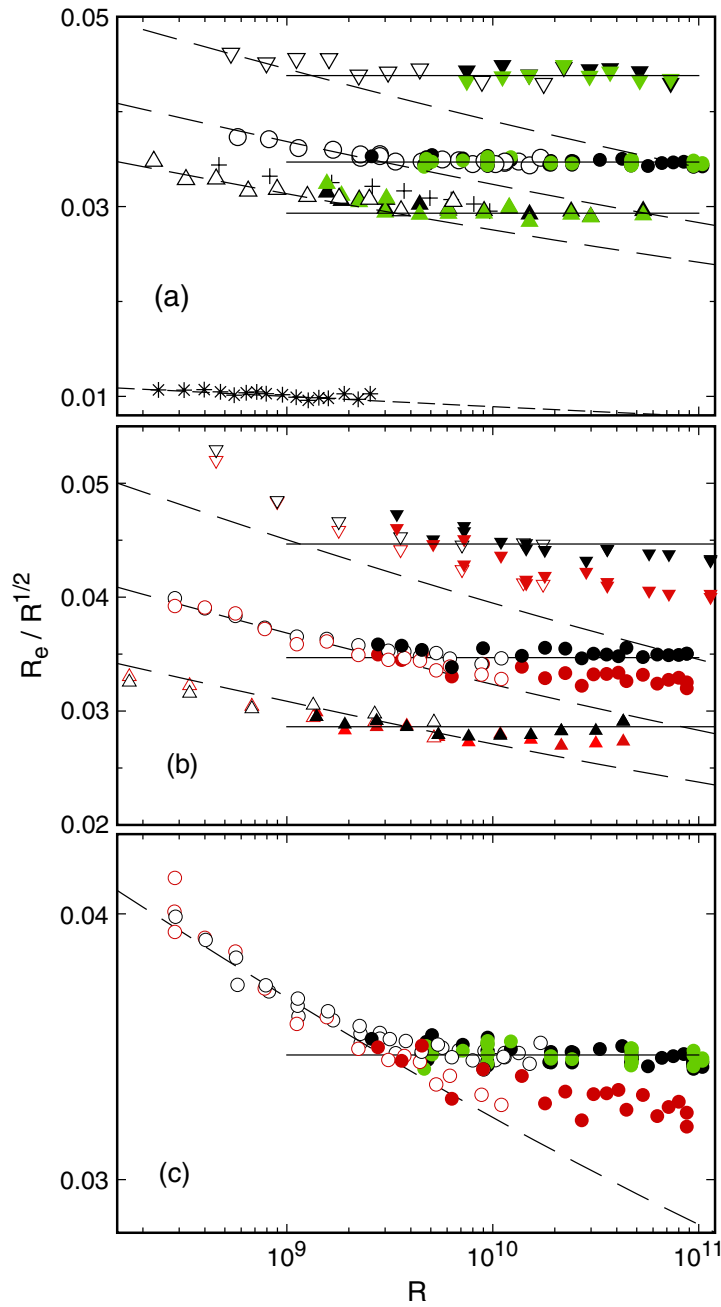
Figure 5. Reduced Reynolds numbers in the form of $R_e/R^{1/2}$ for high-resolution plots on log-linear scales. (a) $R_e^{p,\text{cc}}$ (black symbols) and $R_e^{p,\text{ac}}$ (green symbols) for $\sigma = 4.38$ (circles), $\sigma = 5.55$ (up-pointing triangles), and $\sigma = 3.32$ (down-pointing triangles). Crosses: R_e^u from [16], $\sigma \simeq 5.4$. Dashed lines (from top to bottom): GL predictions for $\sigma = 3.32, 4.38, 5.55$, and 28.9. Stars: R_e^ω for 2-propanol at 40 °C, $\sigma = 28.9$. (b) $R_e^{p,\text{cc}}$ (black symbols) and R_e^ω (red symbols) for $\sigma = 4.38$ (circles), $\sigma = 5.68$ (up-pointing triangles) and $\sigma = 3.26$ (down-pointing triangles). Dashed lines (from top to bottom): GL predictions for $\sigma = 3.26, 4.38, 5.68$. (c) Higher-resolution plot of all the Reynolds numbers for $\sigma = 4.38$, with symbols as in (a) and (b). For all plots the open symbols are for the medium sample and the solid symbols for the large sample.
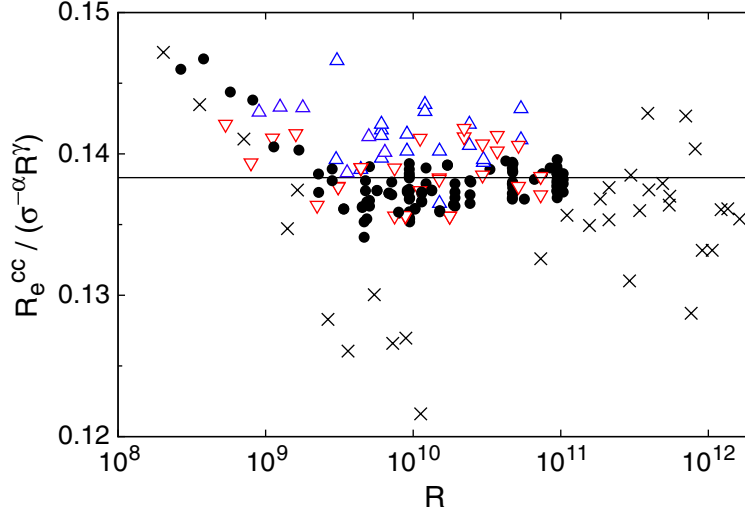
Figure 6. The reduced Reynolds number $R_e^{p,\text{cc}}/(\sigma^{-\alpha}R^\gamma)$ as a function of R. Red down-pointing triangles: $\sigma = 3.26$. Black circles: $\sigma = 4.38$. Blue up-pointing triangles: $\sigma = 5.68$. Solid line: the fit coefficient $R_{e,0}$. Crosses: R_e^p from figure 1 of [35].

scaling in R suddenly changed to about $1/2$. At the largest R measured, the data are about 15% higher than the GL prediction.

Figure 5(b) compares $R_e^{p,\text{cc}}$ (black symbols) with the twisting-oscillation Reynolds number R_e^ω (red symbols). The data are for $\sigma = 3.26$, 4.38, and 5.68. These data were taken from different runs than the data in figure 5(a), hence the slightly different values of σ. The data for $R_e^{p,\text{cc}}$ and R_e^ω are in agreement within the resolution of the experiment for $R < R^*$, which means that the frequencies f_0 and $1/\mathcal{T}_p$ are equal in this range. For $R > R^*$, R_e^ω is larger than the GL prediction but smaller than $R_e^{p,\text{cc}}$. This shows that not only does the power-law scaling of the Reynolds numbers change at R^*, but the two measures of the Reynolds number no longer give the same result above R^*.

The results shown in figures 5(a) and (b) are given in numerical form (tables A.1–A.13) in the appendix. There we no longer distinguish between $R_e^{p,\text{cc}}$ and $R_e^{p,\text{ac}}$ and present both as R_e^p.

The measured $R_e^{p,\text{cc}}$ for $R > R^*$ were fitted by the combined power law given by equation (6) for $R > R^*$ and $3.26 \leq \sigma \leq 5.68$. This yielded $R_{e,0} = 0.138 \pm 0.007$, the Prandtl exponent $\alpha = 0.82 \pm 0.01$, and the Rayleigh exponent $\gamma = 0.493 \pm 0.002$. The Reynolds number is plotted in the reduced form $R_e^{p,\text{cc}}/(\sigma^{-\alpha}R^\gamma)$ in figure 6 to better see deviations from the fit.

Data from Sun and Xia [35] for water with $\sigma = 4.3$ are also shown. These authors obtained a frequency from the power spectrum of a temperature signal from a thermistor inserted through the side wall at mid-height, and the Reynolds number was calculated using the same normalization as in equation (13). At mid-height the twisting mode should not be observable. Thus their measurements should be recording the plume motion and their results should correspond to our R_e^p. The data from their larger cell had $R_e^p \propto R^{1/2}$, in agreement with ours above R^*. Their smaller-cell data are consistent with our results
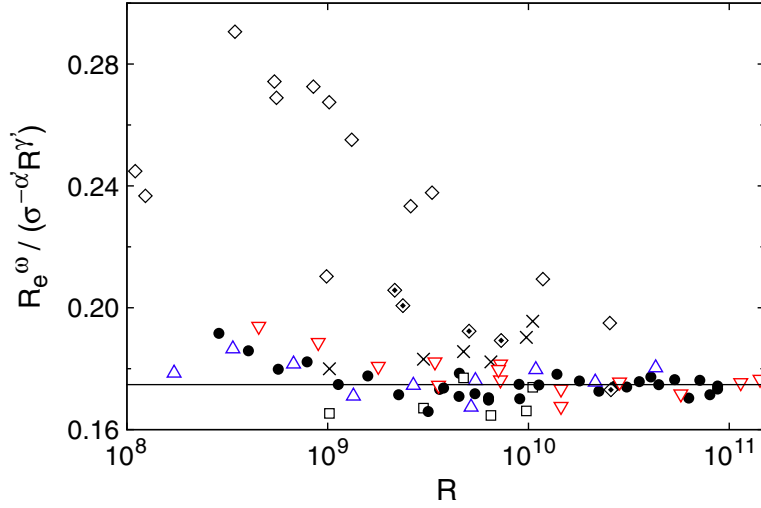
Figure 7. The reduced twisting-oscillation Reynolds number $R_e^\omega/(\sigma^{-\alpha'}R^{\gamma'})$ as a function of R. Red down-pointing triangles: $\sigma = 3.26$. Black circles: $\sigma = 4.38$. Blue up-pointing triangles: $\sigma = 5.68$. Solid line: the fit coefficient $R'_{e,0}$. Reynolds numbers $2L^2/\nu\tau_v$ (squares) and $2L^2/\nu\tau_0$ (crosses) from figure 16 of [45] are shown as well. They correspond to the oscillation frequency of the horizontal LSC speed (squares) and direction (crosses) near the top plate. Open diamonds: Reynolds numbers $2L^2 f/\nu$ corresponding to the oscillation of the velocity magnitude near the side wall in the plume region from figure 8 of [15]; these data were taken with various fluids with $3 \lesssim \sigma \lesssim 1200$. The diamonds with dots inside correspond to the reference [15] data obtained with water with $3 \lesssim \sigma \lesssim 5.5$.

below R^* and with the GL prediction. Sun and Xia suggest that the scaling change near R^* is due to a change in the LSC path-length as R changes. Their results also suggest that R^* for their samples may be somewhat higher than our $R^* \simeq 3 \times 10^9$.

Niemela *et al* [28] measured the Reynolds number corresponding to the plume speed using a pair of sensors with a slight vertical separation at the mid-height and near the side wall of their container in the range $5 \times 10^6 < R < 10^{13}$. They fit a power law for the scaling of $R_e^p(R)$ to the data, and they reported an exponent of $1/2$. However, they had only about one data point per decade and so did not precisely determine how that scaling exponent changed with R.

Similarly, the measured R_e^ω was fitted by the combined power law given in equation (7) for $R > R^*$ and $3.26 \leq \sigma \leq 5.68$. This yielded $R'_{e,0} = 0.17 \pm 0.03, \alpha' = 0.81 \pm 0.03$, and $\gamma' = 0.480 \pm 0.006$. The data are plotted in reduced form $R_e^\omega/(\sigma^{-\alpha'}R^{\gamma'})$ in figure 7.

Xi *et al* [45] used particle-image velocimetry measurements of the horizontal flow velocity and direction near the top plate of a water-filled cylindrical container. They found an oscillation of the spatially averaged flow orientation which presumably is the twisting oscillation (although the direction of flow near the bottom plate was not measured). The period was taken to be the peak time τ_0 of the AC of the flow orientation, from which one can obtain a Reynolds number $R_e^\omega = 2L^2/\nu\tau_0$. They also found an oscillation in the magnitude of the horizontal flow speed, although it is unclear if this signal is due to the twisting oscillation or the plume circulation. The period τ_v was found from the peak of
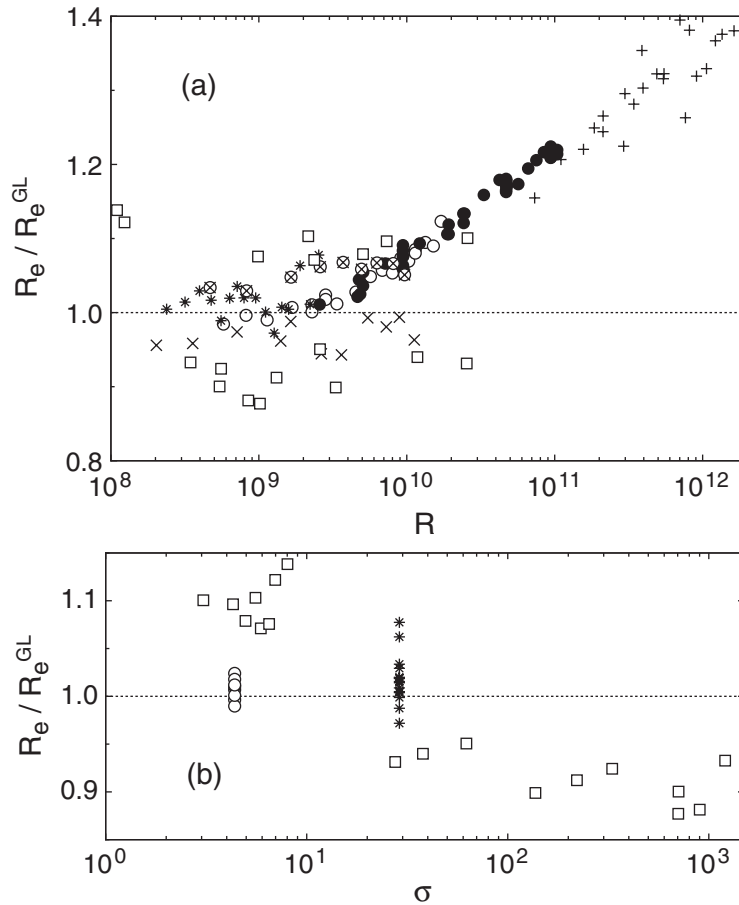
Figure 8. Reynolds numbers from various sources, divided by the GL prediction. Open circles: this work, medium sample, $\sigma = 4.38$. Solid circles: this work, large sample, $\sigma = 4.38$. Stars: this work, small sample, 2-propanol, $\sigma = 29.8$. Plusses: from figure 1 of [35], 100 cm sample, $\sigma = 4.3$. Crosses: from figure 1 of [35], 19.3 cm sample, $\sigma = 4.3$. Circles with crosses: from [16], $\sigma = 5.4$. Squares: from [15], $5.6 \leq \sigma \leq 1206$.

the AC of the flow speed, from which one can obtain a Reynolds number $2L^2/\nu\tau_v$. The Reynolds numbers corresponding to both sets of values from figure 16 of [45] are shown in figure 7 for comparison with our data.

Lam *et al* [15] used laser Doppler velocimetry to measure the flow velocity in cylindrical containers using various fluids covering a wide range of Prandtl numbers $3 \lesssim \sigma \lesssim 1200$. The magnitude of the vertical flow velocity near the sidewall in the plume region had an oscillation frequency f_0 and Reynolds number $2L^2 f_0/\nu$. These data come from figure 8 of [15], and are shown in figure 7. Their data, obtained by using alcohols covering a wide range of σ, do not agree with our σ-scaling. Lam *et al* pointed out that a single scaling exponent did not work for the whole range of σ that they covered.

For a better comparison to the GL prediction, figure 8(a) shows Reynolds numbers from various sources, divided by the GL prediction as a function of R, which clearly shows the transition away from the GL prediction for $R > R^*$. Figure 8(b) shows some of the
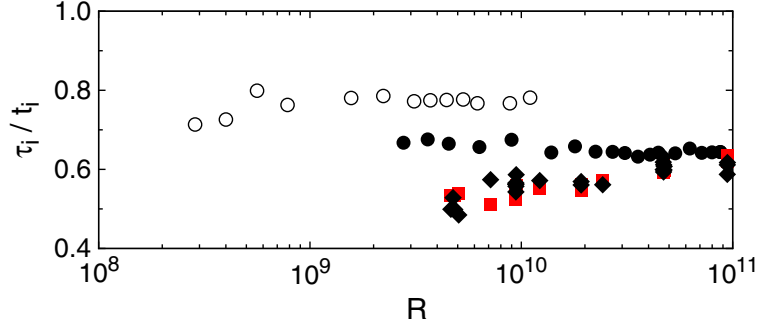
Figure 9. Normalized half-widths of Gaussian correlation-function peaks as a function of R. Open circles: medium sample. Solid symbols: large sample. Circles: τ_1^{cc}/t_1^{cc}. Squares: $2\tau_1^{ac}/t_2^{ac}$. Diamonds: $2\tau_2^{ac}/t_2^{ac}$.

same data as a function of σ for $R < R^*$. The data from [15] for different fluids seem to deviate from the GL prediction. For $\sigma \simeq 4$ they are larger than the GL value and our data by about 10%. For $\sigma = \mathcal{O}(10^3)$ they are lower than the GL value. It seems unlikely that the parameters of the GL model could be adjusted so as to agree better with the high-σR_e data while maintaining agreement with extensive Nusselt-number measurements and with the present R_e-measurements at small σ. More measurements at large σ are clearly needed.

3.4. Half-widths of the correlation-function peaks

The half-widths of the Gaussian peaks of correlation functions like those shown in figure 1 in principle contain information about the temporal distribution of plumes and thus should be relevant to models of plume dynamics such as the one proposed by Villermaux [44]. Figure 9 gives half-widths τ_i normalized by corresponding peak times t_i. We focus first on the circles, which are for the ratios τ_1^{cc}/t_1^{cc} derived from fits of equation (12) to the data for the CCs. They do not reveal any R-dependence, indicating that the half-widths grow with R at the same rate as the characteristic time t_1^{cc} and thus as the Reynolds number $R_e^{p,cc}$. The medium sample yields results that are about 20% larger than those from the large sample. The reason for this modest but real difference is not known to us.

From fits of equation (11) to the data for the ACs one obtains both τ_1^{ac} and τ_2^{ac}. The former is the half-width of the peak at the origin, i.e. at $t = 0$, and the latter is the peak at time t_2^{ac}. As we saw in figure 5, the timescales t_1^{cc} and t_2^{ac} differ by a factor of two and yield the same values for the Reynolds numbers $R_e^{p,cc}$ and $R_e^{p,ac}$ when the definitions equations (13) and (14) are used. This suggests that for a comparison with τ_1^{cc}/t_1^{cc} it is appropriate to use $t_2^{ac}/2$ as the timescale for the normalization. Therefore we show $2\tau_1^{ac}/t_2^{ac}$ and $2\tau_2^{ac}/t_2^{ac}$ as solid squares and diamonds respectively in figure 9. With this normalization one sees that the half-widths of the ACs differ only very little from those of the CCs. Perhaps even more surprising is that the peaks of the ACs at $t = 0$ have the *same* half-widths within experimental resolution as the peaks at t_2^{ac}.
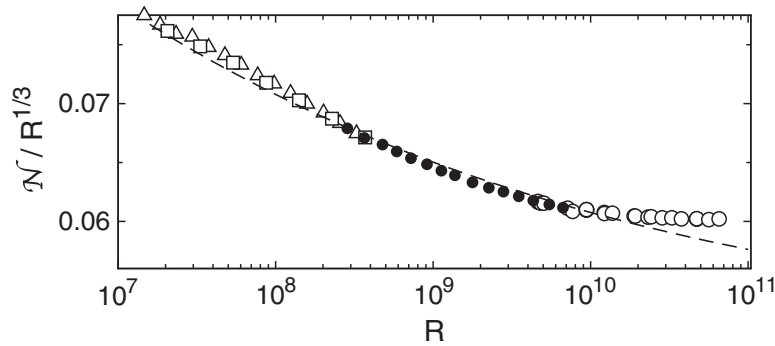
Figure 10. The reduced Nusselt number $\mathcal{N}/R^{1/3}$ as a function of R for $\sigma = 4.38$ [38]. Dashed line: GL prediction. Open circles: large sample. Solid circles: medium sample. Open squares and triangles: two different runs for the small sample containing water with $\sigma = 4.38$.

3.5. Nusselt number

It is interesting to note that a deviation of experimental results for the Nusselt number [38] from the GL prediction was found at large R that is similar to that for the Reynolds number. This is illustrated in figure 10 where we show the reduced Nusselt number $\mathcal{N}/R^{1/3}$ as a function of R. There are deviations from the prediction [32] (dashed line) for $R \gtrsim 10^{10}$, which is somewhat higher than the value of $R^* \simeq 3 \times 10^9$ for the Reynolds number. For $R \gtrsim 10^{10}$ one finds to a good approximation that $\mathcal{N} \sim R^{1/3}$.

3.6. Kinetic energy-dissipation

From measurements of R_e and $\mathcal{N}$ as a function of R one can compute the global average of the kinetic energy-dissipation $\epsilon_u(R_e)$, which is given by the exact relation [46][6], [31]

$$\epsilon_u = (\mathcal{N} - 1)R/\sigma^2. \tag{15}$$

At sufficiently large R the dissipation in the bulk should dominate over that in the boundary layers, and in that case one expects $\epsilon_u \sim R_e^3$ [31]. We saw above that the experimental data at large R yield approximately $\mathcal{N} \sim R^{1/3}$ and $R_e^p \sim R^{1/2}$. If we use R_e^p as the relevant Reynolds number, this leads to $\epsilon_u \sim (R_e^p)^{8/3}$, in disagreement with the expectation for the bulk-dominated dissipation[7]. In order to explore this issue more quantitatively, we show in figure 11 the reduced dissipation $\epsilon_u/(R_e^p)^{8/3}$, which according to the above approximate argument is independent of R_e^p for R_e^p sufficiently large. Indeed we find that the data for $R_e^p \gtrsim 2000$ are consistent with $\epsilon_u = 22.0(R_e^p)^{8/3}$, in disagreement with the expectation for a bulk-dominated region. We believe that the most likely explanation of this predicament is that R_e^p (and for that matter R_e^ω) is not the Reynolds number that is relevant to the argument that yields $\epsilon_u \sim R_e^3$. It would be most interesting to measure $R_e^{v_{max}}$ or R_e^u and $\mathcal{N}$ in the regime $R \gtrsim 10^{10}$ and to see what R_e-dependence of ϵ_u this would yield.

---

[6] Siggia E D in [1].

[7] We are grateful to Siegfried Grossmann for calling our attention to this problem.
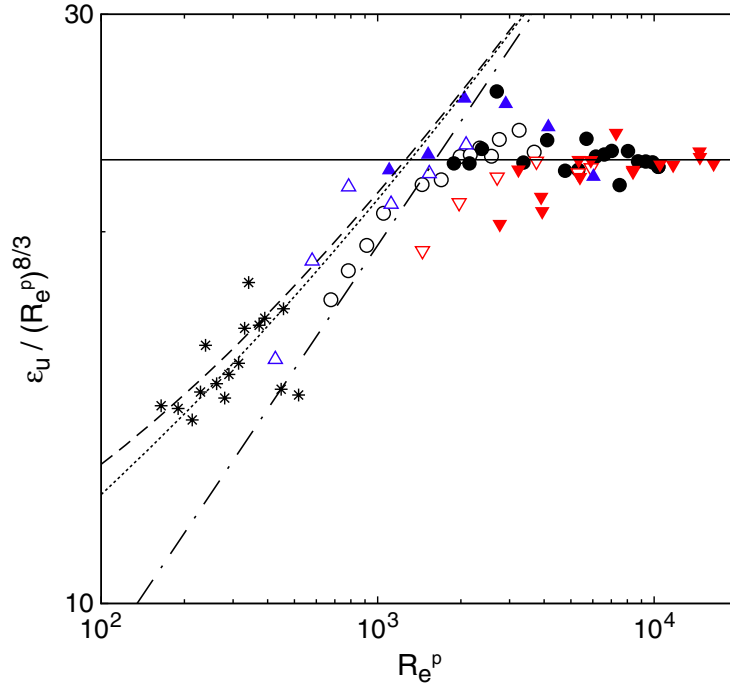
Figure 11. The reduced average kinetic energy-dissipation $\epsilon_u/(R_e^p)^{8/3}$ as a function of R_e^p. Open symbols: medium sample. Solid symbols: large sample. Up-pointing triangles: $\sigma = 3.3$. Circles: $\sigma = 4.4$. Down-pointing triangles: $\sigma = 5.6$. Stars: $\sigma = 28.9$. Solid horizontal line: $\epsilon_u = 22.0(R_e^p)^{8/3}$. Dashed–dotted line: $\epsilon_u = 1.95(R_e^p)^3$. Dotted line: GL prediction for $\sigma = 3.3$. Short dashed line: GL prediction for $\sigma = 28.9$.

For $R_e^p \lesssim 2000$ the experimental data at all Prandtl numbers are consistent with the GL prediction, as shown by their scatter about the dotted and dashed lines in the figure. Here one sees again the excellent agreement with the predicted Prandtl-number dependence over the range $3 \lesssim \sigma \lesssim 30$. The dashed–dotted line in the figure corresponds to $\epsilon_u \sim R_e^3$. One sees that both the data and the GL prediction tend toward the R_e^3-dependence as R_e increases up to R^*.

4. Summary and conclusions

In this paper new measurements of the Reynolds number R_e^p based on a plume turnover time $\mathcal{T}_p$ and of the Reynolds number R_e^ω based on the large-scale circulation oscillation-frequency for $\Gamma = 1$ cylindrical samples were presented over the Rayleigh-number range $2 \times 10^8 \lesssim R \lesssim 10^{11}$ and the Prandtl-number range $3.3 \lesssim \sigma \lesssim 29$. For $R < R^* \simeq 3 \times 10^9$ both were proportional to $R^{0.46}$ and agreed well with each other and with the prediction by Grossmann and Lohse [13]. This provides further support for the GL model in that parameter range. For $R > R^*$ the Reynolds number based on the plume turnover time is represented well by $R_e^p = 0.138\sigma^{-0.82}R^{0.493}$, which differs from the GL prediction. The Reynolds number R_e^ω for the twisting oscillation of the LSC for $R > R^*$ could be fitted

by $R_e^\omega = 0.17\sigma^{-0.81}R^{0.480}$, which differs from both the GL prediction and the result for R_e^p. These measurements suggest a qualitative change in the flow for $R > R^*$ that causes not only the deviation from the GL model, but also a transition to a regime where the two Reynolds numbers no longer agree with each other. It may well be that it is not possible to describe the LSC quantitatively by a unique Reynolds number in this large-R regime.

The average kinetic energy-dissipation ϵ_u, when computed from measurements of the Nusselt number $\mathcal{N}$ and of R_e^p, agrees well with the prediction of GL and with the expected asymptotic proportionality to $(R_e)^3$ when $R < R^* \simeq 3 \times 10^9$. However, at large $R \gtrsim R^* \epsilon_u$ disagrees with the expected proportionality to $(R_e)^3$ and the GL prediction. Instead, to a good approximation the data yield $\epsilon_u \sim (R_e)^{8/3}$. We presume that the problem arises because R_e^p is not the appropriate Reynolds number for the computation of ϵ_u when $R > R^*$.

Acknowledgments

Appendix. Numerical values of the data shown in figures 5(a) and (b)

Table A.1. Reduced Reynolds numbers $R_e^p/R^{1/2}$ as a function of R. Medium sample, $\sigma = 3.32$ (open down-pointing triangles, figure 5(a)).

R	$R_e^p/R^{1/2}$	R	$R_e^p/R^{1/2}$	R	$R_e^p/R^{1/2}$
1.113×10^9	0.0456	8.855×10^9	0.0432	1.602×10^9	0.0456
2.234×10^9	0.0438	1.767×10^{10}	0.0430	7.958×10^8	0.0451
4.420×10^9	0.0445	3.101×10^9	0.0442	5.350×10^8	0.0461

Table A.2. Reduced Reynolds numbers $R_e^p/R^{1/2}$ as a function of R. Large sample, $\sigma = 3.32$ (solid down-pointing triangles, figure 5(a)).

R	$R_e^p/R^{1/2}$	R	$R_e^p/R^{1/2}$	R	$R_e^p/R^{1/2}$
7.309×10^{10}	0.0430	5.170×10^{10}	0.0442	1.501×10^{10}	0.0438
3.712×10^{10}	0.0445	2.950×10^{10}	0.0444	2.214×10^{10}	0.0449
7.480×10^9	0.0443	7.309×10^{10}	0.0434	5.170×10^{10}	0.0433
1.114×10^{10}	0.0449	3.712×10^{10}	0.0442	2.950×10^{10}	0.0437
1.501×10^{10}	0.0438	7.480×10^9	0.0432		
2.214×10^{10}	0.0447	1.114×10^{10}	0.0437		

Table A.3. Reduced Reynolds numbers $R_e^p/R^{1/2}$ as a function of R. Medium sample, $\sigma = 4.38$ (open circles, figure 5(a)).

R	$R_e^p/R^{1/2}$	R	$R_e^p/R^{1/2}$	R	$R_e^p/R^{1/2}$
1.141×10^{10}	0.0346	5.687×10^9	0.0350	7.977×10^9	0.0345
9.104×10^9	0.0348	1.137×10^9	0.0361	1.029×10^{10}	0.0345
6.845×10^9	0.0349	3.376×10^9	0.0348	1.334×10^{10}	0.0348
4.519×10^9	0.0347	5.763×10^8	0.0373	1.511×10^{10}	0.0344
2.282×10^9	0.0351	8.191×10^8	0.0371	1.708×10^{10}	0.0352
2.281×10^9	0.0355	1.677×10^9	0.0360	2.825×10^9	0.0353
1.141×10^{10}	0.0348	2.825×10^9	0.0355		

Table A.4. Reduced Reynolds numbers $R_e^p/R^{1/2}$ as a function of R. Large sample, $\sigma = 4.38$ (solid circles, figure 5(a)).

R	$R_e^p/R^{1/2}$	R	$R_e^p/R^{1/2}$	R	$R_e^p/R^{1/2}$
2.576×10^9	0.0353	4.696×10^{10}	0.0343	4.710×10^{10}	0.0346
4.642×10^9	0.0344	4.710×10^{10}	0.0346	4.714×10^{10}	0.0348
4.753×10^9	0.0352	4.711×10^{10}	0.0348	4.642×10^9	0.0342
4.842×10^9	0.0345	4.713×10^{10}	0.0345	9.445×10^{10}	0.0348
5.055×10^9	0.0348	4.734×10^{10}	0.0346	1.222×10^{10}	0.0352
5.068×10^9	0.0354	4.743×10^{10}	0.0346	7.155×10^9	0.0348
7.155×10^9	0.0351	5.677×10^{10}	0.0343	9.426×10^9	0.0352
9.416×10^9	0.0345	6.624×10^{10}	0.0346	9.420×10^9	0.0344
9.419×10^9	0.0349	7.510×10^{10}	0.0346	4.842×10^9	0.0348
9.420×10^9	0.0351	8.454×10^{10}	0.0347	1.040×10^{11}	0.0346
9.426×10^9	0.0353	9.393×10^{10}	0.0343	1.040×10^{11}	0.0345
9.430×10^9	0.0348	9.397×10^{10}	0.0344	1.919×10^{10}	0.0346
9.454×10^9	0.0343	9.397×10^{10}	0.0344	1.919×10^{10}	0.0346
9.457×10^9	0.0343	9.399×10^{10}	0.0346	4.753×10^9	0.0350
1.222×10^{10}	0.0349	9.402×10^{10}	0.0347	9.457×10^9	0.0347
1.877×10^{10}	0.0344	9.432×10^{10}	0.0342	9.435×10^{10}	0.0347
1.919×10^{10}	0.0348	9.435×10^{10}	0.0345	4.734×10^{10}	0.0344
1.919×10^{10}	0.0344	9.435×10^{10}	0.0344	9.430×10^9	0.0351
2.415×10^{10}	0.0348	9.440×10^{10}	0.0343	4.696×10^{10}	0.0346
2.427×10^{10}	0.0344	9.445×10^{10}	0.0346	9.416×10^9	0.0352
2.459×10^{10}	0.0348	1.040×10^{11}	0.0344	4.743×10^{10}	0.0349
3.315×10^{10}	0.0349	1.040×10^{11}	0.0342	4.694×10^{10}	0.0349
4.243×10^{10}	0.0350	9.432×10^{10}	0.0343	4.693×10^{10}	0.0343
4.693×10^{10}	0.0344	2.427×10^{10}	0.0345	9.427×10^9	0.0347
4.694×10^{10}	0.0349	5.056×10^9	0.0347		

Table A.5. Reduced Reynolds numbers $R_e^p/R^{1/2}$ as a function of R. Medium sample, $\sigma = 5.55$ (open up-pointing triangles, figure 5(a)).

R	$R_e^p/R^{1/2}$	R	$R_e^p/R^{1/2}$	R	$R_e^p/R^{1/2}$
6.427×10^9	0.0305	4.537×10^8	0.0329	1.258×10^9	0.0310
3.586×10^9	0.0296	2.258×10^8	0.0348	2.515×10^9	0.0308
1.794×10^9	0.0309	3.237×10^8	0.0328		
8.969×10^8	0.0318	6.491×10^8	0.0316		

Table A.6. Reduced Reynolds numbers $R_e^p/R^{1/2}$ as a function of R. Large sample, $\sigma = 5.55$ (solid up-pointing triangles, figure 5(a)).

R	$R_e^p/R^{1/2}$	R	$R_e^p/R^{1/2}$	R	$R_e^p/R^{1/2}$
5.374×10^{10}	0.0295	1.564×10^9	0.0315	9.074×10^9	0.0293
2.990×10^{10}	0.0289	6.087×10^9	0.0296	1.201×10^{10}	0.0300
1.508×10^{10}	0.0292	2.245×10^9	0.0307	2.402×10^{10}	0.0292
3.003×10^9	0.0298	1.842×10^9	0.0306	3.045×10^9	0.0309
4.415×10^9	0.0302	5.374×10^{10}	0.0291	1.564×10^9	0.0324
6.092×10^9	0.0298	2.990×10^{10}	0.0289	6.087×10^9	0.0297
9.074×10^9	0.0295	1.508×10^{10}	0.0284	2.245×10^9	0.0305
1.201×10^{10}	0.0298	3.003×10^9	0.0294	1.842×10^9	0.0312
2.402×10^{10}	0.0295	4.415×10^9	0.0292		
3.045×10^9	0.0307	6.092×10^9	0.0293		

Table A.7. Reduced Reynolds numbers $R_e^\omega/R^{1/2}$ as a function of R. Small sample, $\sigma = 28.9$ (stars, figure 5(a)).

R	$R_e^\omega/R^{1/2}$	R	$R_e^\omega/R^{1/2}$	R	$R_e^\omega/R^{1/2}$
2.380×10^8	0.010 68	7.140×10^8	0.010 47	1.590×10^9	0.009 79
3.170×10^8	0.010 66	7.940×10^8	0.010 28	1.900×10^9	0.010 27
3.970×10^8	0.010 71	9.520×10^8	0.010 18	2.220×10^9	0.009 69
4.760×10^8	0.010 48	1.110×10^9	0.009 91	2.540×10^9	0.010 27
5.550×10^8	0.010 12	1.270×10^9	0.009 58		
6.350×10^8	0.010 38	1.430×10^9	0.009 86		

Table A.8. Reduced Reynolds numbers $R_e^p/R^{1/2}$ (black open down-pointing triangles, figure 5(b)) and $R_e^\omega/R^{1/2}$ (red open down-pointing triangles, figure 5(b)) as a function of R. Medium sample, $\sigma = 5.68$.

R	$R_e^p/R^{1/2}$	$R_e^\omega/R^{1/2}$	R	$R_e^p/R^{1/2}$	$R_e^\omega/R^{1/2}$
4.534×10^8	0.0529	0.0520	8.973×10^8	0.0485	0.0484
1.786×10^9	0.0466	0.0459	3.565×10^9	0.0453	0.0442
7.088×10^9	0.0446	0.0424	1.408×10^{10}	0.0448	0.0413
1.755×10^{10}	0.0447	0.0411			

Table A.9. Reduced Reynolds numbers $R_e^p/R^{1/2}$ (black solid down-pointing triangles, figure 5(b)) and $R_e^\omega/R^{1/2}$ (red solid down-pointing triangles, figure 5(b)) as a function of R. Large sample, $\sigma = 5.68$.

R	$R_e^p/R^{1/2}$	$R_e^\omega/R^{1/2}$	R	$R_e^p/R^{1/2}$	$R_e^\omega/R^{1/2}$
1.141×10^{11}	0.0432	0.0403	5.740×10^{10}	0.0438	0.0406
2.843×10^{10}	0.0432	0.0422	1.452×10^{10}	0.0443	0.0412
7.262×10^9	0.0458	0.0451	3.421×10^9	0.0473	0.0461
7.252×10^9	0.0462	0.0429	1.452×10^{10}	0.0447	0.0415
7.165×10^{10}	0.0438	0.0402	3.597×10^{10}	0.0442	0.0410
3.597×10^{10}	0.0442	0.0413	1.789×10^{10}	0.0441	0.0419
1.141×10^{11}	0.0433	0.0400	1.096×10^{10}	0.0448	0.0436
5.134×10^9	0.0451	0.0447			

Table A.10. Reduced Reynolds numbers $R_e^p/R^{1/2}$ (black open circles, figure 5(b)) and $R_e^\omega/R^{1/2}$ (red open circles, figure 5(b)) as a function of R. Medium sample, $\sigma = 4.38$.

R	$R_e^p/R^{1/2}$	$R_e^\omega/R^{1/2}$	R	$R_e^p/R^{1/2}$	$R_e^\omega/R^{1/2}$
1.116×10^9	0.0365	0.0359	2.224×10^9	0.0358	0.0349
4.435×10^9	0.0348	0.0344	8.829×10^9	0.0341	0.0332
1.100×10^{10}	0.0346	0.0328	7.819×10^8	0.0373	0.0372
5.624×10^8	0.0384	0.0386	4.000×10^8	0.0390	0.0391
2.858×10^8	0.0399	0.0392	1.564×10^9	0.0363	0.0361
3.110×10^9	0.0353	0.0345	6.200×10^9	0.0346	0.0339
3.716×10^9	0.0352	0.0347	5.310×10^9	0.0351	0.0336

Table A.11. Reduced Reynolds numbers $R_e^p/R^{1/2}$ (black solid circles, figure 5(b)) and $R_e^\omega/R^{1/2}$ (red solid circles, figure 5(b)) as a function of R. Large sample, $\sigma = 4.38$.

R	$R_e^p/R^{1/2}$	$R_e^\omega/R^{1/2}$	R	$R_e^p/R^{1/2}$	$R_e^\omega/R^{1/2}$
8.980×10^9	0.0355	0.0342	1.795×10^{10}	0.0356	0.0329
2.706×10^{10}	0.0346	0.0322	3.564×10^{10}	0.0350	0.0332
4.454×10^{10}	0.0356	0.0326	4.067×10^{10}	0.0348	0.0334
3.090×10^{10}	0.0350	0.0332	2.244×10^{10}	0.0355	0.0333
1.386×10^{10}	0.0348	0.0339	2.772×10^9	0.0358	0.0350
8.734×10^{10}	0.0350	0.0320	8.737×10^{10}	0.0350	0.0325
7.995×10^{10}	0.0349	0.0329	7.140×10^{10}	0.0349	0.0327
6.274×10^{10}	0.0349	0.0324	5.356×10^{10}	0.0347	0.0332
4.533×10^9	0.0354	0.0350	3.610×10^9	0.0357	0.0345
6.336×10^9	0.0339	0.0330			

Table A.12. Reduced Reynolds numbers $R_e^p/R^{1/2}$ (black open up-pointing triangles, figure 5(b)) and $R_e^\omega/R^{1/2}$ (red open up-pointing triangles, figure 5(b)) as a function of R. Medium sample, $\sigma = 3.26$.

R	$R_e^p/R^{1/2}$	$R_e^\omega/R^{1/2}$	R	$R_e^p/R^{1/2}$	$R_e^\omega/R^{1/2}$
6.760×10^8	0.0302	0.0304	3.370×10^8	0.0316	0.0322
1.343×10^9	0.0305	0.0294	2.670×10^9	0.0297	0.0290
5.178×10^9	0.0290	0.0276	1.718×10^8	0.0325	0.0330

Table A.13. Reduced Reynolds numbers $R_e^p/R^{1/2}$ (black solid up-pointing triangles, figure 5(b)) and $R_e^\omega/R^{1/2}$ (red solid up-pointing triangles, figure 5(b)) as a function of R. Large sample, $\sigma = 3.26$.

R	$R_e^p/R^{1/2}$	$R_e^\omega/R^{1/2}$	R	$R_e^p/R^{1/2}$	$R_e^\omega/R^{1/2}$
$1.393\,36 \times 10^9$	0.029 49	0.029 90	$2.728\,99 \times 10^9$	0.029 15	0.028 60
$5.441\,50 \times 10^9$	0.027 91	0.027 73	$1.087\,78 \times 10^{10}$	0.027 86	0.027 98
$2.150\,99 \times 10^{10}$	0.028 24	0.026 96	$4.300\,69 \times 10^{10}$	0.029 09	0.027 33
$1.912\,57 \times 10^9$	0.028 82	0.028 31	$3.821\,59 \times 10^9$	0.028 61	0.028 72
$7.633\,62 \times 10^9$	0.027 77	0.027 27	$1.530\,45 \times 10^{10}$	0.027 91	0.027 49
$3.164\,77 \times 10^{10}$	0.028 27	0.027 17			

References

[1] For recent reviews, see for instance Siggia E D, 1994 *Annu. Rev. Fluid Mech.* **26** 137
    Kadanoff L, 2001 *Phys. Today* **54** (8) 34
    Ahlers G, Grossmann S and Lohse D, 2002 *Physik J.* **1** (2) 31
[2] Krishnamurty R and Howard L N, 1981 *Proc. Nat. Acad. Sci. USA* **78** 1981
[3] Sano M, Wu X-Z and Libchaber A, 1989 *Phys. Rev.* A **40** 6421
[4] Castaing B, Gunaratne G, Heslot F, Kadanoff L, Libchaber A, Thomae S, Wu X-Z, Zaleski S and
    Zanetti G, 1989 *J. Fluid Mech.* **204** 1
[5] Ciliberto S, Cioni S and Laroche C, 1996 *Phys. Rev.* E **54** R5901
[6] Chavanne X, Chillá F, Chabaud B, Castaing B and Hébral B, 2001 *Phys. Fluids* **13** 1300
[7] Qiu X-L and Tong P, 2001 *Phys. Rev.* E **64** 036304
[8] Funfschilling D and Ahlers G, 2004 *Phys. Rev. Lett.* **92** 194502
[9] Sun C, Xia K-Q and Tong P, 2005 *Phys. Rev.* E **72** 026302
[10] Tsuji Y, Mizuno T, Mashiko T and Sano M, 2005 *Phys. Rev. Lett.* **94** 034501
[11] See, for instance, van Doorn E, Dhruva B, Sreenivasan K and Cassella V, 2000 *Phys. Fluids* **12** 1529
[12] See, for instance, Glatzmaier G, Coe R, Hongre L and Roberts P, 1999 *Nature* **401** 885
[13] Grossmann S and Lohse D, 2002 *Phys. Rev.* E **66** 016305
[14] Qiu X-L and Tong P, 2001 *Phys. Rev. Lett.* **87** 094501
[15] Lam S, Shang X-D, Zhou S-Q and Xia K-Q, 2002 *Phys. Rev.* E **65** 066306
[16] Qiu X-L and Tong P, 2002 *Phys. Rev.* E **66** 026308
[17] Howard R and LaBonte B, 1980 *Astrophys. J.* **239** L33
[18] Dumberry M and Bloxham J, 2004 *Geophys. J. Int.* **159** 417
[19] Resagk C, du Puits R, Thess A, Dolzhansky F V, Grossmann S, Fontenele Araujo F and Lohse D, 2006
     Phys. Fluids **18** 095105
[20] Funfschilling D, Brown E and Ahlers G, 2007 *J. Fluid Mech.* submitted
[21] Heslot F, Castaing B and Libchaber A, 1987 *Phys. Rev.* A **36** 5870
[22] Takeshita T, Segawa T, Glazier J and Sano M, 1996 *Phys. Rev. Lett.* **76** 1465
[23] Cioni S, Ciliberto S and Sommeria J, 1997 *J. Fluid Mech.* **335** 111
[24] Qiu X-L, Yao S H and Tong P, 2000 *Phys. Rev.* E **61** R6075
[25] Qiu X L, Shang X D, Tong P and Xia K Q, 2004 *Phys. Fluids* **16** 412
[26] Libchaber A, 1987 *Proc. R. Soc.* A **413** 63
[27] Chavanne X, Chillá F, Castaing B, Hébral B, Chabaud B and Chaussy J, 1997 *Phys. Rev. Lett.* **79** 3648
[28] Niemela J J, Skrbek L, Sreenivasan K R and Donnelly R J, 2001 *J. Fluid Mech.* **449** 169
[29] Ahlers G, Brown E and Nikolaenko A, 2006 *J. Fluid Mech.* **557** 347
[30] Kraichnan R, 1962 *Phys. Fluids* **5** 1374
[31] Grossmann S and Lohse D, 2000 *J. Fluid Mech.* **407** 27
[32] Grossmann S and Lohse D, 2001 *Phys. Rev. Lett.* **86** 3316
[33] Grossmann S and Lohse D, 2004 *Phys. Fluids* **16** 4462
[34] Niemela J J and Sreenivasan K R, 2003 *Europhys. Lett.* **62** 829
[35] Sun C and Xia K-Q, 2005 *Phys. Rev.* E **72** 067302
[36] Ahlers G and Xu X, 2001 *Phys. Rev. Lett.* **86** 3320
[37] Xia K Q, Lam S and Zhou S Q, 2002 *Phys. Rev. Lett.* **88** 064501
[38] Funfschilling D, Brown E, Nikolaenko A and Ahlers G, 2005 *J. Fluid Mech.* **536** 145
[39] Brown E, Nikolaenko A, Funfschilling D and Ahlers G, 2005 *Phys. Fluids* **17** 075108
[40] de Bruyn J R, Bodenschatz E, Morris S W, Trainoff S P, Hu Y, Cannell D S and Ahlers G, 1996 *Rev. Sci.
     Instrum.* **67** 20043
[41] Brown E and Ahlers G, 2006 *J. Fluid Mech.* **568** 351
[42] Brown E and Ahlers G, 2007 *Europhys. Lett.* **80** 14001
[43] Tilgner A, Belmonte A and Libchaber A, 1993 *Phys. Rev.* E **47** R2253
[44] Villermaux E, 1995 *Phys. Rev. Lett.* **75** 4618
[45] Xi H-D, Zhou Q and Xia K-Q, 2006 *Phys. Rev.* E **73** 056312
[46] Shraiman B I and Siggia E D, 1990 *Phys. Rev.* A **42** 3650

J. Stat. Mech. (2007) P10005